Serb. Astron. J. № 212 (2026), 47 - 66
DOI: https://doi.org/10.2298/SAJ2612047F

UDC 524.7–337 + 524.6–76
Original scientific paper

TESTING PERIOD DIAGNOSTICS ON QUASAR PERIODIC CANDIDATES IN THE ERA OF LARGE SURVEYS

Marta Fatović[1,2,3], Andjelka B. Kovačević[4], Dragana Ilić[4,5] and Demetra De Cicco[1]

[1] *Dipartimento di Fisica "Ettore Pancini", Università di Napoli Federico II, Via Cintia 80126, Naples, Italy*
E–mail: *marta.fatovic@unina.it*

[2] *Rudjer Bošković Institute, Bijenička cesta 54, 10000 Zagreb, Croatia*

[3] *INAF – Osservatorio Astronomico di Capodimonte, Via Moiariello 16, 80131 Naples, Italy*

[4] *Department of Astronomy, Faculty of Mathematics, University of Belgrade Studentski trg 16, 11000 Belgrade, Serbia*

[5] *Hamburger Sternwarte, Universität Hamburg, Gojenbergsweg 112, D-21029 Hamburg, Germany*

(Received: February 2, 2026; Accepted: May 27, 2026)

SUMMARY: We assess the variability of four quasars previously identified as periodically variable quasar candidates. We analyze the extended light curves which now include Pan-STARRS1 (PS1), additional Zwicky Transient Facility (ZTF) observations together with archival Dark Energy Survey (DES) data that were not considered in the previous study, substantially increasing both the temporal baseline and sampling. Periodicity is re-evaluated using two independent period-search methods, enabling a direct comparison of the inferred periods across different data sets and temporal blocks, which are tested for the effects of cadence or stochastic (red-noise) nature. In addition, we investigate the structure function, phase-folded color–magnitude behavior, and timescale dependent color variability to assess whether the apparent periodic signals are accompanied by other coherent (chromatic) variability. This combined analysis presents a possible methodology for the assessment of future large multi-band time-domain surveys, which should aim to probe the robustness, persistence, and physical nature of the possible periodicity in faint quasars.

Key words. Galaxies: quasars: general – Methods: statistical – Methods: data analysis – Techniques: photometric – Surveys

1. INTRODUCTION

Active galactic nuclei (AGN) are intrinsically variable across a broad range of wavelengths and timescales from hours to decades, reflecting physical processes in compact regions that cannot be spatially resolved in distant quasars (e.g., Ulrich et al. 1997, Vanden Berk et al. 2004, Ivezic et al. 2004, Falocco et al. 2015, De Cicco et al. 2019, Paolillo and Papadakis 2025). In optical, the quasar variability is commonly described as a stochastic, red-noise process, typically modeled using the damped random walk (DRW) or related Gaussian-process formulations, with more general extensions such as the damped harmonic oscillator (DHO) framework recently proposed to capture a wider range of variability behaviours (e.g., Kelly et al. 2009, Kozłowski et al. 2010, MacLeod et al. 2010, Zu et al. 2013, Ivezić and MacLeod 2014, Stone et al. 2022, Yu et al. 2025). While these models successfully reproduce the statistical properties of quasar ensembles, they also highlight a fundamental challenge for time-domain studies: apparent periodic signals spanning only a few cycles can arise naturally from red-noise variability—particularly in sparsely sampled or noisy light

curves—and can, therefore, be misidentified as true, physically driven periodicity (e.g., Vaughan et al. 2016, Krishnan et al. 2021, Witt et al. 2022, Chen et al. 2024).

Periodic or quasi-periodic variability in quasars does not uniquely point to a single physical origin and can arise from several processes intrinsic to accretion onto supermassive black holes. Variability on characteristic timescales may be produced by instabilities and oscillatory modes in accretion disks, including thermal and limit-cycle instabilities, which can generate quasi-periodic signals without long-term phase coherence (e.g., Janiuk and Czerny 2011, Śniegowska et al. 2025). Geometric effects such as disk warping or jet precession can also introduce periodic or quasi-periodic modulation of the observed emission, often with evolving amplitude and phase (e.g., Graham et al. 2015, Liska et al. 2018, Britzen et al. 2023). Recent reassessments have emphasized that many reported periodic quasar candidates are consistent with such transient or stochastic behavior rather than stable, long-lived periodic drivers (e.g., Deng 2026).

Within this broader context, a primary motivation for searching for periodic or quasi-periodic AGN variability is the potential identification of sub-parsec supermassive black hole binaries (SMBHBs), which are the expected outcomes of galaxy mergers (Begelman et al. 1980, De Rosa et al. 2019). In such systems, periodic signals may arise from orbital modulation of circumbinary accretion flows (e.g., D'Orazio et al. 2013, Charisi et al. 2016, Liao et al. 2021), relativistic Doppler boosting of emission from a minidisc, producing nearly achromatic, phase-coherent variability (D'Orazio et al. 2015, Graham et al. 2015, Charisi et al. 2018), or from geometric and radiative-transfer effects such as the disc or jet precession that can generate a quasi-periodic behavior without long-term stability (e.g., Farris et al. 2014, Qian et al. 2018, El-Badry et al. 2026). These mechanisms need not produce strictly sinusoidal or persistent signals, further complicating the interpretation of photometric periodicity.

Spectroscopic monitoring plays a central role in testing physical interpretations of candidate periodic quasars. Multi-epoch spectroscopy probes the broad-line region (BLR) and enables tests of binary or disk-like BLR scenarios through velocity offsets and time-dependent changes in broad emission-line profiles (e.g., Boroson and Lauer 2009, Shen and Loeb 2010, Runnoe et al. 2016, Guo et al. 2019a,b). Importantly, the binary interpretation relies not only on the presence of double-peaked lines, but also on the temporal evolution of the line profile itself—including systematic changes in shape and centroid—rather than on the flux-only "changing-look" variability (e.g., Eracleous and Halpern 1994, Lewis et al. 2010, Popović et al. 2014, Fatović et al. 2025).

A systematic search for periodic variability in the SDSS Stripe 82 standard-star catalog by Fatović et al. (2023, hereafter F23) identified five faint ($\sim$21–22 mag) quasar candidates with plausible periodic signals, by using multiple independent photometric methods. One of these sources has since been included in a dedicated multi-epoch spectroscopic monitoring campaign as a candidate close binary supermassive black hole (CB-SMBH). Although the photometric periodicity of this object was subsequently questioned based on light-curve diagnostics alone (Rigamonti et al. 2025), follow-up spectroscopy revealed a time-variable, double-peaked Mg II emission-line profile, underscoring the physical complexity of the source and illustrating how such behavior could remain undiscovered if the candidate were discarded solely on photometric grounds (Fatović et al. 2025). The extreme faintness of the sample places these candidates in a regime where sparse temporal sampling, large photometric uncertainties, and red-noise–dominated variability substantially increase the likelihood of false-positive detections in light-curve–based periodicity searches. At the same time, this example demonstrates that potentially valuable candidates may be prematurely discarded when assessed using a single diagnostic. Given the high observational cost of spectroscopic monitoring for faint AGN, this motivates a reassessment of the photometric evidence for the remaining candidates using a combination of complementary diagnostics. Moving beyond standard period searches alone, additional tools such as structure function (SF), color variability and color–magnitude analyses can provide independent constraints on the physical origin of the variability and help identify the most robust targets for future spectroscopic follow-up.

SF is a standard, model-independent tool for characterizing the AGN variability and has extensively been applied in recent time-domain surveys to study variability amplitudes and characteristic timescales (e.g. Kasliwal et al. 2015, Simm et al. 2016, Kozłowski 2016, Caplar et al. 2017, Sánchez-Sáez et al. 2018, De Cicco et al. 2022). Recent work has emphasized that the SF measurements are sensitive to sampling effects and red-noise processes, particularly in the context of periodicity searches (e.g. Charisi et al. 2016, Graham et al. 2017, Kovačević et al. 2021, Paolillo and Papadakis 2025). As shown by Kovačević et al. (2021), when a light curve contains a periodic component, the same oscillatory signal can manifest at long timescales in SF, producing local minima at integer multiples of the period, nP. However, SF alone does not constitute a proof of periodicity; rather, it provides supporting evidence, as the signal is typically distorted by the observational noise, irregular sampling, and the presence of a dominant stochastic variability component.

Color variability provides another independent and physically informative probe. Quasars typically exhibit bluer-when-brighter (BWB) behavior, with the amplitude and coherence of color variability depending on timescale and emission components (e.g., Schmidt et al. 2012, Sun et al. 2014, Chen et al.

2024). Some SMBHB scenarios predict variability that is close to achromatic in the optical—such as geometric modulation or relativistic Doppler boosting—producing phase-coherent flux variations with relatively weak color evolution (D'Orazio et al. 2015, Charisi et al. 2018). Importantly, periodic or quasi-periodic behavior may be transient, appearing only during limited epochs, allowing such systems to evade searches that require long-term coherence (e.g., Vaughan et al. 2016, Krishnan et al. 2021, El-Badry et al. 2026).

In this context, we also introduce a new, phase-resolved, color diagnostics as a physically motivated way to assess the nature of candidate periodic variability, drawing inspiration from analogous techniques long employed in the study of periodically variable stars. In stellar variability studies, phase-folded color–magnitude diagrams have been used to trace coherent temperature and radius changes over a cycle, revealing ordered evolutionary paths that are tightly locked to the pulsation phase (e.g., Madore 1985, Sesar et al. 2010, Szabó et al. 2014). Adopting this concept for AGN, rather than characterizing color behavior through time-averaged trends or ensemble correlations (e.g., Schmidt et al. 2012, Chen et al. 2024, Sudan et al. 2025), we explicitly examine whether color evolution is phase-locked to a candidate photometric period. Ordered, repeatable trajectories in color–magnitude space provide direct evidence that spectral and flux variations are governed by the same underlying clock, a behavior that is difficult to reproduce with purely stochastic variability. Crucially, because this method does not require long-term phase coherence across the full light curve, it remains sensitive to transient or episodic periodic behavior. The phase-folded color–magnitude analysis therefore complements traditional periodicity searches and extends a well-established stellar variability diagnostic into the AGN regime, offering a scalable tool for identifying physically coherent variability in large time-domain surveys.

This approach will become particularly powerful in the era of the Legacy Survey of Space and Time (LSST) at the Vera C. Rubin Observatory. LSST will provide unprecedented depth and cadence for faint AGN, reaching single-visit depths of r $\sim$ 24.5 mag and coadded depths of r $\sim$ 27.5 mag over its 10-year survey (LSST Science Collaboration et al. 2009, Ivezić et al. 2019). Although LSST will not always obtain strictly simultaneous multi-band observations, its observing strategy will frequently enable quasi-simultaneous color measurements through closely spaced visits. For faint sources like those studied here, this combination of depth and cadence will substantially reduce current ambiguities and make color–phase diagnostics a practical tool for identifying intrinsically periodic or quasi-periodic AGN, and for prioritizing spectroscopic follow-up.

In this work, we analyze the remaining four candidates from F23 using extended multi-survey light curves and color-based variability diagnostics, with the aim of determining whether the reported periodicity is intrinsic, and whether it is transient or persistent in time. While F23 focused primarily on SDSS data, we analyze expanded and updated light curves combining SDSS (York et al. 2000), Pan-STARRS1 Data Release 2 (PS1 DR2, Chambers et al. 2016, Flewelling et al. 2020), Zwicky Transient Facility Data Release 23 (ZTF DR23, Masci et al. 2019), and the newly added Dark Energy Survey Data Release 2 (DES DR2, Dark Energy Survey Collaboration et al. 2016, Abbott et al. 2021) observations. The extended temporal baseline, improved sampling, and increased availability of multi-band data allow us to revisit and reassess the robustness of the proposed periodic signals, including tests of cadence and red-noise effects. Understanding whether such variability is driven by stochastic accretion processes, geometric modulation, or more exotic scenarios, such as CB-SMBH, is essential, as these systems provide unique insight into the AGN structure and evolution and represent potential electromagnetic counterparts and targets for future gravitational-wave facilities.

This paper is organized as follows. In Section 2, we describe the data used in this work. Section 3 outlines the analysis methods and presents the corresponding results. In Section 4, we discuss each candidate individually and explore its possible interpretation. Finally, in Section 5, we summarize our main conclusions.

2. DATA

F23 carried out period analysis on the SDSS light curves using astropy's Lomb–Scargle implementation, with the PS1 DR2 and ZTF DR11 data included for visual comparison. In this work, we update both the light curves and the analysis by incorporating the most recent ZTF observations from the current data release (DR23), and by including archival DES DR2 photometry to improve the temporal cadence.

All photometric measurements were calibrated to the SDSS *gri* filter system following the same procedure as in F23, as given in Eq. 1:

$$\mathrm{SURVEY}_{\mathrm{corr}} = \mathrm{SURVEY} + \langle \mathrm{SURVEY} \rangle - \langle \mathrm{SDSS} \rangle, \quad (1)$$

where $\mathrm{SURVEY}_{\mathrm{corr}}$ is the corrected magnitude, obtained by shifting the original magnitude by the median difference between the survey in question and SDSS. The candidate identifiers (ID = 10, 20, 25, 27) are adopted from F23 for consistency.

Table 1 summarizes the general properties of the sources, including their coordinates, periods reported in F23, median magnitudes in each band, and basic information on the light curve cadence. The full light curves span long baselines of up to $\sim$25 yr with several tens to over one hundred epochs per band, but the sampling is highly heterogeneous, with median cadences ranging from a few days in SDSS to

several tens or hundreds of days in DES and ZTF. The data quality varies across the individual surveys and their combinations, as reflected in the different baselines, sampling, and number of epochs. The SDSS light curves are relatively sparse, with $\sim$ 27 epochs per band, while DES provides denser coverage ($\sim$ 60–70 epochs) over long baselines ($\gtrsim$ 1800 days). ZTF further extends the temporal coverage (up to $\sim$ 2000 days), albeit with uneven sampling across bands, and PS1 contributes intermediate baselines and cadence. $F_{\rm var}$ is the fractional variability amplitude, computed from the sample variance after subtraction of the mean squared photometric uncertainty and normalized by the mean magnitude. The $F_{\rm var}$ are generally modest, with $F_{\rm var} \sim 10^{-3}$–10^{-2} in most bands and datasets, and show only weak band dependence. Despite the differences in data quality between individual blocks, $F_{\rm var}$ remain broadly consistent, indicating that the observed variability is intrinsic to the sources rather than driven by survey-specific effects.

2.1. SDSS

We use the SDSS Stripe 82 light curves constructed by Thanjavur et al. (2021), who extended the standard star light curves of Ivezić et al. (2007) using the post-2007 SDSS imaging data from Data Release 15. These light curves provide multi-epoch photometry in the *ugriz* bands with improved temporal coverage, typically comprising ∼20–50 observations per source depending on position within Stripe 82. The data are optimized for studies of long-period, low-amplitude variability in optically non-variable sources. For more details on the data construction and usage, see the original works by Ivezić et al. (2007) and Thanjavur et al. (2021), or the summary in F23.

In F23 and in this study, the same SDSS photometric data were used and we restrict the analysis to the *gri* filters, which typically provide the highest signal-to-noise ratio.

2.2. PS1 DR2

We use multi-epoch photometry from the PS1 DR2, which provides calibrated light curves in the *grizy* filter system over a multi-year baseline. The PS1 data offer sparse, but valuable temporal sampling that complements the other surveys used in this work. In F23 and in this study, the same PS1 DR2 photometric data were used and we limit the analysis to the *gri* filters.

2.3. ZTF

In F23, light curves were constructed using the ZTF Data Release 11 (DR11), whereas in this study, we update them with observations from the latest public release, DR23, which extends the temporal baseline and adds the most recent data points. The ZTF data releases are issued regularly, and are well suited for studies of optical variability due to their high observing cadence.

To reduce photometric scatter and improve the quality of the time-series data, we bin the ZTF magnitudes into 3-day intervals. For each bin, we compute a weighted mean magnitude using the individual measurement uncertainties. This approach enhances the signal-to-noise ratio of the light curves while preserving the underlying variability on longer timescales.

2.4. DES

We incorporate photometric data from the DES DR2, which were not used in F23, to extend and complement the existing light curves. The DES DR2 observations partially overlap in time with the PS1 and ZTF data, providing an independent consistency check. The DES photometry is binned into 3-day intervals following the same procedure applied to the ZTF data.

3. ANALYSIS AND RESULTS

We investigate the temporal variability of the sources by focusing on two complementary aspects: the identification of periodic signals in the light curves and the associated color variability.

3.1. Period analysis

We first derive candidate periods using the full temporal baseline of the available light curves. Given their long durations (∼7000–9000 days), we then investigate whether the detected periodic modulation is persistent or transient by subdividing the data into temporal blocks and repeating the period analysis in each segment. This approach allows us to assess the stability of the inferred periods over time and to test whether periodic behavior is present only during specific phases of the light curve, as has been suggested in F23.

Because the SDSS observations are temporally well separated from the remainder of the data, they are treated as Block 1. Block 2 consists of the PS1 and DES light curves, which are grouped together because they probe comparable epochs and provide complementary coverage in terms of cadence and depth. When considered individually, each survey contains relatively few measurements, but together they improve sampling without significantly extending the temporal baseline. The ZTF data are assigned to Block 3, as they exhibit the largest scatter on average. For these faint sources, ZTF also has the largest photometric uncertainties and its constraining power may, therefore, be limited for some objects. These differences in data quality are intrinsic to the multi-survey dataset and can affect the sensitivity to

Table 1: Source and light curve properties of each object given for full combined data set and individual data blocks.

	ID = 10	ID = 20	ID = 25	ID = 27
RA [deg]	14.629833	20.572870	23.537440	44.539858
Dec [deg]	-0.622042	-0.422368	-0.839078	-0.206044
$P_{\rm Fatovic+23}$	297	466	300	480
z	0.98	2.48	1.37	0.98
(g, r, i) [mag]	(21.2, 20.9, 20.8)	(21.6, 21.5, 21.4)	(21.8, 21.4, 21.2)	(22.0, 21.7, 21.5)
Full light curves				
(N_g, N_r, N_i)	(113, 174, 159)	(59, 103, 54)	(75, 71, 72)	(70, 76, 69)
baseline (g,r,i)	(8036, 8031, 7561)	(8055, 8847, 8393)	(9476, 7737, 7325)	(9504, 9175, 7005)
$\Delta t_{\rm median}$ (g,r,i)	(9.8, 5.0, 5.4)	(15.8, 12.9, 15.9)	(15.4, 16.9, 7.9)	(9.0, 8.0, 4.0)
$F_{\rm var}$ (g,r,i)	(0.008, 0.004, 0.007)	(0.017, 0.014, 0.014)	(0.007, 0.006, 0.006)	(0.018, 0.015, 0.013)
SDSS				
(N_g, N_r, N_i)	(27, 27, 27)	(38, 38, 36)	(48, 48, 51)	(49, 49, 46)
baseline (g,r,i)	(2238, 2238, 2238)	(3349, 3349, 3349)	(2277, 3349, 3349)	(3346, 3346, 3346)
$\Delta t_{\rm median}$ (g,r,i)	(8.0, 8.0, 8.0)	(11.9, 11.9, 11.9)	(6.1, 6.9, 6.1)	(4.0, 4.0, 5.0)
$F_{\rm var}$ (g,r,i)	(0.006, 0.006, 0.005)	(0.021, 0.019, 0.016)	(0.006, 0.006, 0.007)	(0.020, 0.017, 0.015)
PS1				
(N_g, N_r, N_i)	(8, 18, 14)	(8, 11, 7)	(7, 9, 12)	(1, 8, 18)
baseline (g,r,i)	(735, 1875, 1447)	(711, 1134, 1423)	(1132, 1504, 736)	(0, 1177, 1402)
$\Delta t_{\rm median}$ (g,r,i)	(6.0, 0.01, 0.9)	(0.01, 3.5, 8.4)	(202.4, 40.9, 0.01)	(–, 101.8, 0.01)
$F_{\rm var}$ (g,r,i)	(0.007, 0.008, 0.006)	(0.012, 0.008, 0.013)	(0.011, 0.006, 0.006)	(–, 0.005, 0.008)
DES				
(N_g, N_r, N_i)	(70, 119, 118)	(11, 8, 8)	(9, 10, 9)	(6, 3, 5)
baseline (g,r,i)	(2316, 2480, 2320)	(1837, 1444, 1831)	(1856, 1856, 1856)	(1541, 440, 1749)
$\Delta t_{\rm median}$ (g,r,i)	(8.0, 4.4, 5.0)	(42.9, 283.3, 336.5)	(191.5, 281.3, 294.7)	(310.2, 219.9, 455.2)
$F_{\rm var}$ (g,r,i)	(0.008, 0.008, 0.007)	(0.004, 0.008, 0.009)	(0.003, 0.002, 0.002)	(0.014, 0.022, 0.011)
ZTF				
(N_g, N_r, N_i)	(8, 10, 0)	(2, 46, 3)	(11, 4, 0)	(14, 16, 0)
baseline (g,r,i)	(728, 777, 0)	(700, 1587, 9)	(2177, 450, 0)	(2231, 1739, 0)
$\Delta t_{\rm median}$ (g,r,i)	(22.0, 26.5, –)	(700.1, 35.3, 4.5)	(177.5, 62.9, –)	(18.0, 28.0, –)
$F_{\rm var}$ (g,r,i)	(0.011, 0.006, –)	(0.007, 0.010, 0)	(0.010, 0.013, –)	(0.009, 0.013, –)
PS1+DES (Block 2)				
(N_g, N_r, N_i)	(78, 137, 132)	(19, 19, 15)	(16, 19, 21)	(7, 11, 23)
baseline (g,r,i)	(3163, 3705, 3176)	(2901, 2924, 2935)	(2901, 2934, 2194)	(2275, 2627, 2568)
$\Delta t_{\rm median}$ (g,r,i)	(8.0, 4.2, 5.0)	(23.9, 19.4, 185.5)	(56.7, 67.3, 27.3)	(351.1, 223.8, 0.01)
$F_{\rm var}$ (g,r,i)	(0.008, 0.008, 0.007)	(0.009, 0.008, 0.011)	(0.007, 0.004, 0.005)	(0.013, 0.010, 0.008)

Notes. RA and Dec are given in decimal degrees; z denotes the spectroscopic redshift; (N_g, N_r, N_i) indicate the number of epochs per band; baseline (g,r,i) is the baseline of the dataset, obtained as the time span between the first and last observation; $\Delta t_{\rm median}$ denotes the median time separation between consecutive observations, providing a robust estimate of the typical sampling cadence; $F_{\rm var}$ is the fractional variability amplitude.

periodic signals in each block. To account for this, we perform the period analysis independently in each block and compare the consistency of the recovered periods and their significance.

The period analysis is carried out using multiple complementary methods, including a Multiband Lomb–Scargle periodogram implemented in the *gatspy* package (VanderPlas and Ivezić 2015) and the Quasar Harmonic eXplorer method (QhX, Kovačević et al. 2018, 2019, 2020, Kovačević et al. 2022) where both methods intrinsically explore phase space through the period search, making them robust against unknown initial phase offsets between segments. A truly persistent periodicity should still yield a consistent period across blocks. In contrast, the transient behavior would manifest as inconsistent period recovery and/or a loss of significance beyond detection thresholds.

3.1.1. Multiband Lomb-Scargle

We apply the multiband Lomb–Scargle (MBLS) method (VanderPlas and Ivezić 2015) to search for periodic variability in the light curves. We initially explored a broad period range of 100–1000 days using the full temporal baseline of the data, appropriate for probing long-timescale variability. This initial search consistently yielded candidate periods clustered between approximately 300 and 500 days. Motivated by this result, we subsequently focussed the period search to the range of 200–600 days when analyzing the individual temporal blocks allowing sufficient flexibility for the algorithms while avoiding an unnecessarily large parameter space. Narrowing the period range reduces sensitivity to spurious long-period solutions that can arise from uneven sampling, seasonal gaps, or long-term trends, and allows for a more robust and stable comparison of period estimates across different subsets of the data. All results are summarized in Table 2, which is divided into four sections: (i) amplitudes, periods, significance, and the bootstrap mean and uncertainty derived from the full dataset; and (ii–iv) the same quantities computed separately for the SDSS (Block 1), PS1+DES (Block 2), and ZTF (Block 3) data.

Fig. 1 shows the light curves of the four candidates in all three bands, combining data from all four surveys. To enable a consistent comparison across surveys and epochs, we over-plot the sinusoidal model corresponding to the best-fit period obtained from a MBLS analysis of the complete data set. Using a single global model provides a common reference for assessing the phase coherence and relative amplitude of the modulation across different bands and surveys, and allows us to visually evaluate whether the apparent variability amplitude remains stable over time.

Table 2: Periods obtained by Multiband Lomb-Scargle method.

	ID = 10	ID = 20	ID = 25	ID = 27
Full light curves:				
Amp(g, r, i) [mag]	(0.6, 0.6, 0.5)	(1.2, 1.0, 1.1)	(0.6, 0.4, 0.4)	(1.2, 1.1, 0.9)
P_{MBLS} [days]	472	421	303	487
Significance	1.00	1.00	1.00	1.00
$P_{\mathrm{boot,\,mean}}$ [days]	459	420	322	430
$P_{\mathrm{boot,\,std}}$ [days]	59	63	53	80
SDSS (Block 1):				
Amp(g, r, i) [mag]	(0.4, 0.3, 0.4)	(1.3, 1.1, 1.1)	(0.5, 0.4, 0.5)	(1.3, 1.1, 1.0)
P_{MBLS} [days]	296*	467	302	479*
Significance	1.00	1.00	1.00	1.00
$P_{\mathrm{boot,\,mean}}$ [days]	350	462	312	455
$P_{\mathrm{boot,\,std}}$ [days]	90	21	39	62
PS1+DES (Block 2):				
Amp(g, r, i) [mag]	(0.6, 0.6, 0.6)	(0.5, 0.6, 0.7)	(0.5, 0.3, 0.4)	(0.7, 0.7, 0.6)
P_{MBLS} [days]	485*,**	267**	360*,**	366*,**
Significance	0.97	0.69	0.86	0.81
$P_{\mathrm{boot,\,mean}}$ [days]	456	317	318	376
$P_{\mathrm{boot,\,std}}$ [days]	90	108	101	97
ZTF (Block 3):				
Amp(g, r, i) [mag]	(0.7, 0.6, -)	(-, 0.8, -)	(0.8, -, -)	(0.8, 1.0, -)
P_{MBLS} [days]	478**	332*	427**	439**
Significance	0.23	1.00	0.81	0.97
$P_{\mathrm{boot,\,mean}}$ [days]	322	368	373	368
$P_{\mathrm{boot,\,std}}$ [days]	112	102	136	86

Notes. Amp(g, r, i) is the robust peak-to-peak variability amplitude, defined as $mag_{95} - mag_5$ of the observed magnitude distribution in each band. P_{MBLS} is the Multiband Lomb–Scargle period. Periods flagged with * are those whose MBLS peaks fall within the vicinity of prominent window-function peaks and may, therefore, be influenced by cadence-related aliases. Periods marked with ** are the ones whose maximum periodogram power did not exceed the 99th percentile of the bootstrap maximum-power distribution and are considered not significant.

We emphasize that the model is intended as an illustrative representation of the dominant periodic component rather than a detailed physical description of the variability.

3.1.2. Window function, false-alarm analysis and testing for red noise

To assess the reliability of the detected periodicities and to identify potential aliases introduced by the temporal sampling, we performed additional diagnostic tests based on the spectral window function and on an empirical false-alarm probability (FAP) estimate. These tests are particularly important given that most of the detected periods lie in the range of approximately 300–500 days, where seasonal sampling could potentially introduce spurious signals. However, the work F23 investigated periodicities over the 100–600 day range and, therefore, the periods we identify are not unexpected within this broader context.

The influence of the observing cadence was evaluated using the window function. Period detections were flagged as potentially affected by cadence-induced aliases if the best-fit period lay within 3% of one year or within a comparable fractional tolerance of other prominent peaks in the window function. This tolerance reflects the finite width of cadence-related features in the window function, which arise from the limited temporal baseline and irregular sampling of the data, and ensures that the periods influenced by such features are identified without encroaching significantly on the overall period range explored (200–600 d). We flag detections whose best-fit periods coincide with prominent peaks in the window function as potentially susceptible to cadence-driven aliases (marked with "*" in Table 2), particularly near the annual observing cycle. We stress that such cases are not necessarily spurious, but warrant cautious interpretation. Fig. 2 provides a visual representation of the sampling cadence for each source in *gri* filters based on the full light curves, showing the 5th–95th percentile range of the cadence distribution together with the measured period and the corresponding 0.3P and 1.2P values indicated.

The statistical significance of the detected periods was quantified using a bootstrap-based FAP. Under the null hypothesis of absence of coherent periodic signal, surrogate light curves were generated by randomly permuting the observed magnitudes within each photometric band, while keeping the observation times, band labels, and photometric uncertainties fixed. For each bootstrap realization, MBLS was recomputed over the same period range, and the maximum power was recorded. FAP was defined as the fraction of bootstrap realizations in which the maximum periodogram power exceeded that of the original data, corresponding to a global false-alarm probability over the scanned period interval. Periodici-

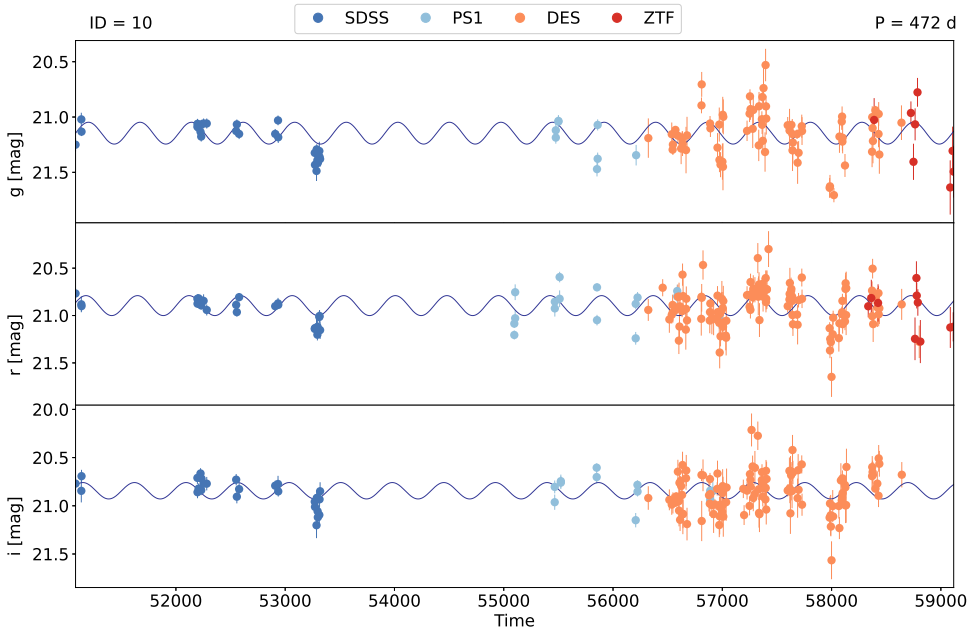

(a)

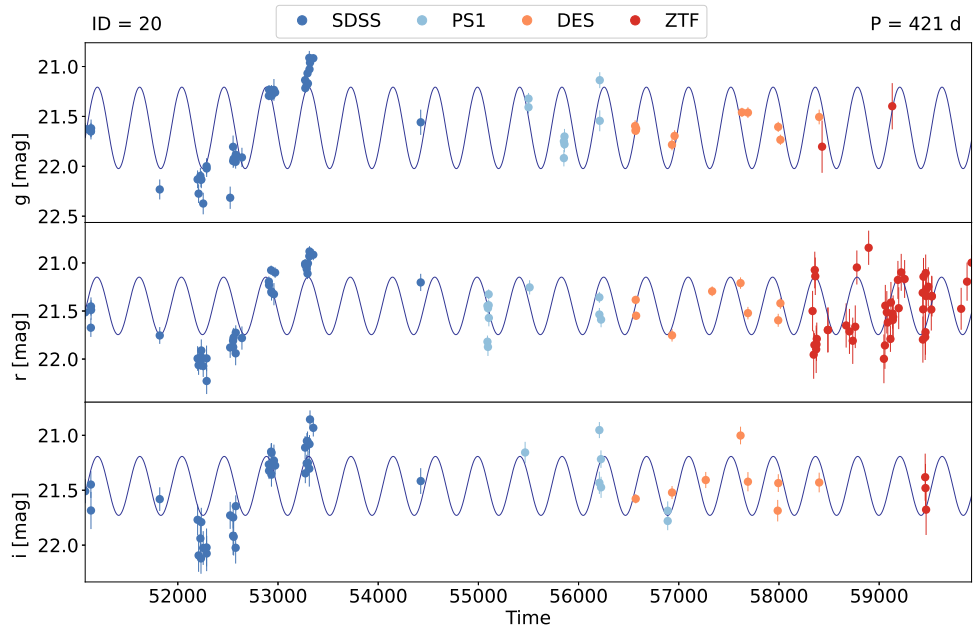

(b)

Fig. 1: *gri* light curves for the four candidates, with over-plotted sinusoidal models corresponding to the best-fit periods derived from MBLS analysis of the complete data set. ID of the object and estimated period are denoted on top of each panel. Different data sets are denoted with different color.

ties were considered significant if their maximum periodogram power exceeded the 99th percentile of the bootstrap maximum-power distribution. The periods marked with a "**" in Table 2 are the ones that did not pass this criterion.

To assess whether the detected periodicities can be attributed to stochastic variability, we tested red-noise null hypothesis. For each source, we estimated the slope of the power spectral density (PSD) and generated 1000 synthetic light curves with a power-law PSD, preserving the original time sampling. For each realization, a MBLS periodogram was computed and the dominant period was recorded. We then measured the fraction of simulations in which the recov-

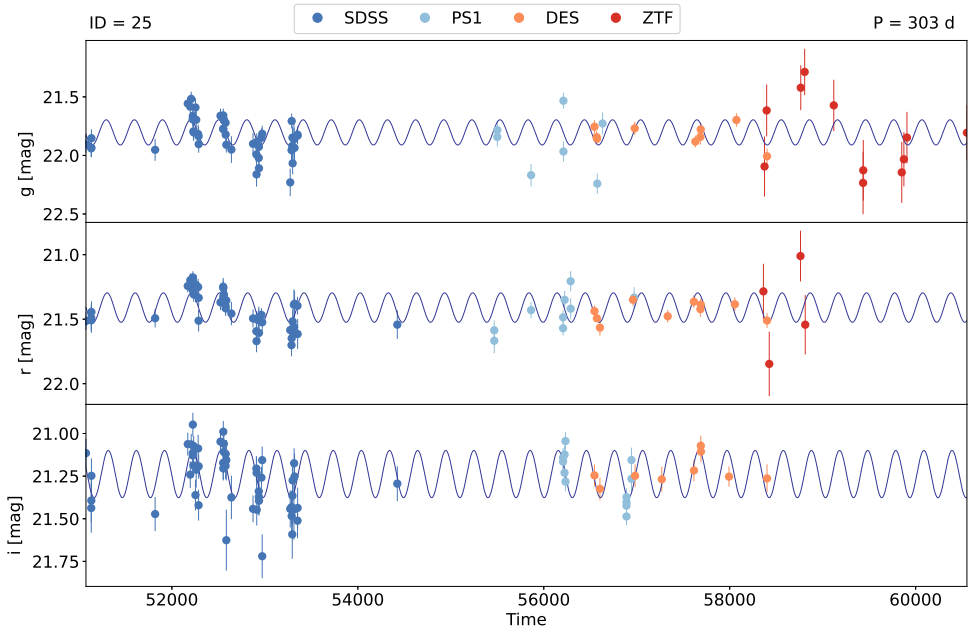

(c)

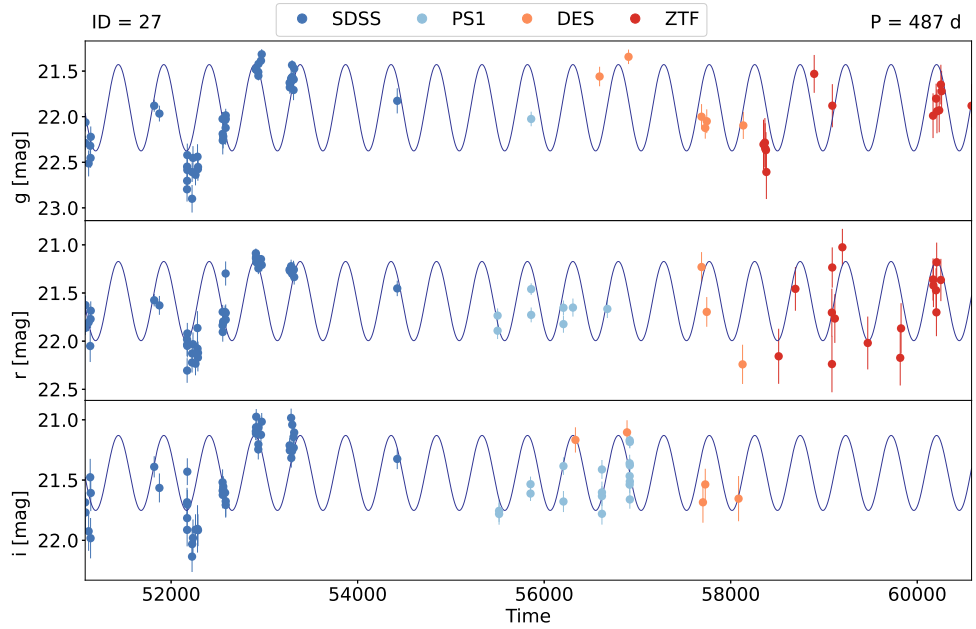

(d)

Fig. 1: Continued.

ered period matches the observed one within a 1%, 5% and 10% tolerance. This fraction quantifies the probability that the observed periodicity arises from red-noise variability. The results are summarised in Table 3.

Object with ID = 10 can be considered a marginal candidate, as the fraction of red-noise realizations reproducing the detected period remains relatively low but increases with tolerance. Similar applies for the source with ID = 20, which shows slightly lower values at the strictest tolerance, suggesting a tentative or suggestive detection, though the significance weakens at larger tolerances. In contrast, ID = 25 exhibits consistently high fractions, particularly at 5% and 10%, indicating that the detected periodicity may be a result of the red-noise nature of the signal. Finally, ID = 27 stands out as a strong candidate, with very low fractions across all tolerance levels, implying that the detected signal is unlikely to be reproduced by red-noise alone.

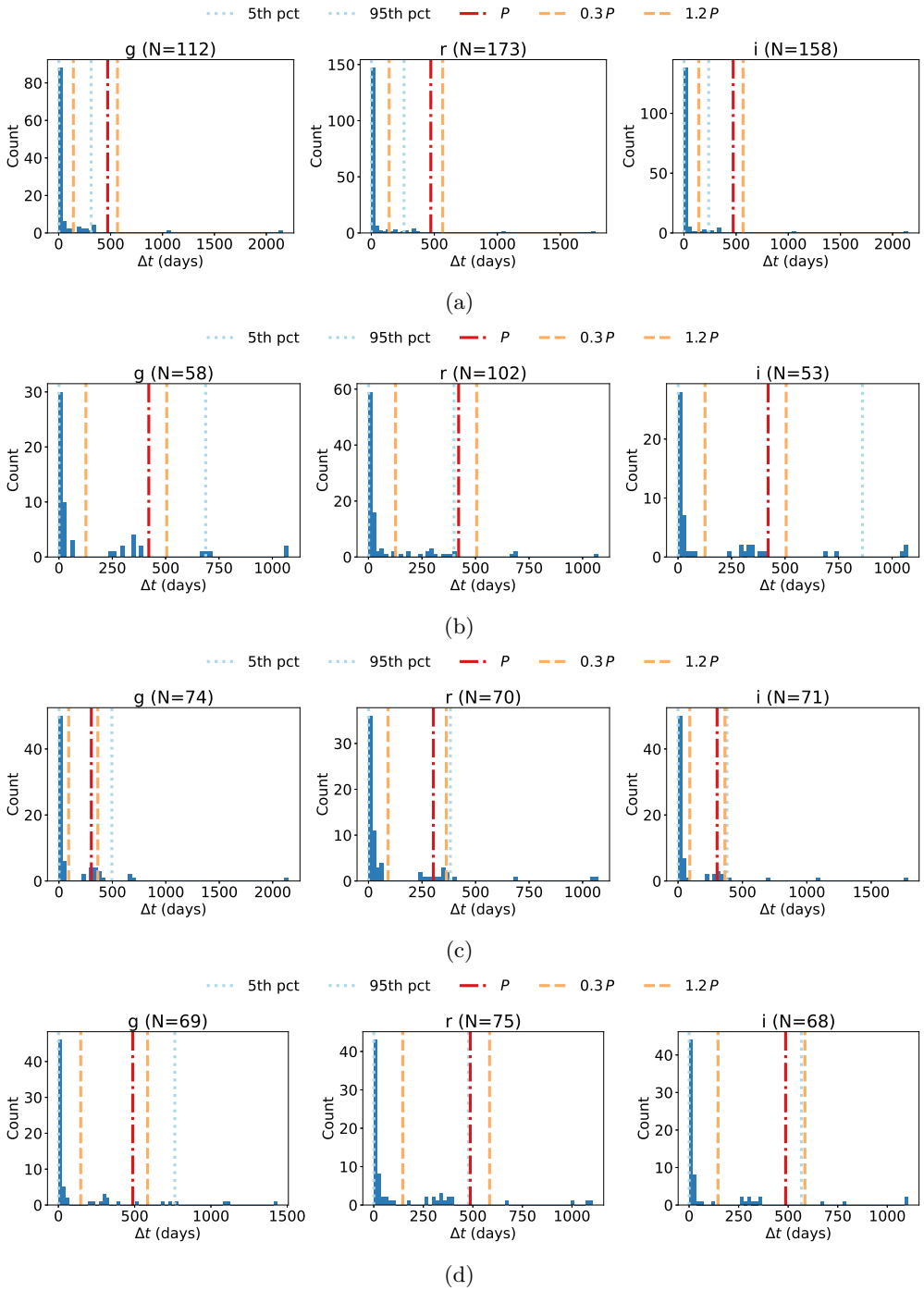

Fig. 2: Sampling cadence (Δt) in the g, r, and i bands for the full light curves of each source. The histograms illustrate the sampling cadence in each filter, with vertical dotted lines marking the 5th and 95th percentiles of the Δt distribution. The measured photometric period P is indicated by the red dashed line, while the orange dashed lines denote $0.3P$ and $1.2P$, highlighting the relation between the characteristic cadence and the candidate periodic timescale. Panels (a)–(d) correspond to IDs 10, 20, 25, and 27, respectively.

3.1.3. Quasar Harmonic eXplorer

To independently verify the periods derived with the MBLS method, we employed the Quasar Harmonic eXplorer (QhX, Kovačević et al. 2018, 2019, 2020, Kovačević et al. 2022) pipeline, which is based on a two-dimensional hybrid time–frequency analysis combining wavelet and correlation-based techniques. This approach enables the detection of coherent periodic signals while accounting for uneven sampling

Table 3: The red-noise false-alarm test from N_{sim} = 1000 cadence- and PSD-matched simulations. The fraction gives the proportion of simulated light curves with a comparable periodic feature within the stated tolerance of the observed period.

	ID = 10	ID = 20	ID = 25	ID = 27
1%	1.6%	0.9%	2.1%	0.3%
5%	5.3%	3.9%	13.4%	1.5%
10%	12.8%	14.4%	35.1%	2.1%

and potential temporal evolution of the frequency. We applied the pipeline only to the full light curves, focusing on correlations between pairs of filters. This analysis was not performed on individual data blocks because QhX is the first tool to explicitly account for the number of data points in the light curves, and empirical tests indicate that a minimum of 80 epochs is required to obtain reliable results (Kovačević et al., in prep.). The resulting periods P_{QhX} are listed in Table 4.

QhX requires a minimum of five frequency grid samples across each arm of the correlation peak in order to compute a stable full-width-at-half-maximum (FWHM)–based uncertainty; when this condition is not satisfied, fallback error estimates are reported. For the detected period P $\simeq$ 432 d of source ID = 10, the cadence sensitivity window spanning 0.3P $\approx$ 130 d to 1.2P $\approx$ 520 d is shown in Fig. 2a. The distribution of inter-observation time gaps is dominated by short separations (Δt < P), providing strong phase anchoring and accounting for the well-constrained lower uncertainty bound. A smaller number of sparse seasonal and survey gaps populate the high-Δt tail of the cadence distribution within the 0.3P–1.2P interval, reducing the effective number of independent phase samples near the correlation maximum. As a result, fewer than the required five frequency grid points are occasionally available on one side of the WWZ peak, leading to asymmetric peak profiles, modest peak broadening, and triggering of fallback uncertainty estimates in a subset of realizations. Importantly, these gaps do not dominate the median cadence, indicating that the detected periodicity is not driven by aliasing but that the precision of the period estimate is limited by incomplete phase coverage. This motivates the use of capped upper error bounds when reporting the period uncertainties.

Objects 20 and 25 exhibit consistent recovered periods across all band pairs using the multiband QhX variant, with high statistical significance and relatively small effective uncertainties, indicating stable cross-band coherence. In contrast, Object 10 shows a $\sim$ 30% discrepancy between the g–r and g–i recovered periods and no significant detection in r–i, consistent with increased sensitivity to cadence gaps and reduced temporal overlap at long periods. Despite a comparable temporal baseline to other candidates, Object 27 exhibits significantly lower effective phase sampling with only $\sim$3–5 measurements per cycle per band. This sparse cadence, combined with large seasonal gaps, prevents robust multiband QhX detection, leading to non-detection under our significance criteria.

3.2. Supporting diagnostics

To further examine the inferred periods, we apply a set of diagnostic techniques to explore whether the detected signals are supported by additional evidence for coherent modulation, as reflected in the structure function, color–magnitude behavior, or timescale-dependent color variability.

3.2.1. Structure function

Kovačević et al. (2021) constructed structure functions for simulated light curves containing periodic signals, using both highly sampled cadences and LSST OpSim cadences. They showed that the same oscillatory signatures appear in the structure functions at timescales corresponding to integer multiples of the input period. In this context, we probe whether similar behavior is present in our observational data.

To quantify the variability amplitude as a function of timescale, we computed SF for each photometric band. To minimize systematic effects arising from heterogeneous cadence and photometric calibration, the analysis was restricted to the SDSS data. SF was computed using an adaptive timescale binning scheme designed to balance statistical robustness and clarity across a wide range of timescales. Timescales were binned logarithmically at short separations with bin width $\Delta\log\,\tau = 0.5$, providing coarse sampling where variability typically rises rapidly. Beyond the transition timescale τ = 200 days, a linear binning with a fixed width of 200 days was adopted, reducing the density of bins at long timescales where pair statistics are high and SF evolves more slowly. Each bin was required to contain a minimum of five epoch pairs to ensure reliable estimates. SF in each bin was calculated as the square root of the mean squared magnitude difference, and uncertainties were estimated from the scatter of pairwise differences within the bin. SF was defined as in Sun et al. (2014):

$$SF(\tau) = \sqrt{\frac{1}{N(\tau)} \sum [m(t+\tau) - m(t)]^2}, \quad (2)$$

and evaluated in logarithmic bins of τ. The maximum timescale was limited to a fixed fraction (0.8) of the total light-curve baseline in order to avoid poorly sampled edge regimes where the number of epoch pairs rapidly decreases and SF estimates become increasingly noisy and biased (e.g. de Vries et al. 2005, Emmanoulopoulos et al. 2010).

Fig. 3 shows the resulting SFs in the *gri* bands. Given the faint magnitudes of the sources and the small number of available epochs, SFs are affected

Table 4: Recovered QhX periods and uncertainties. For each band pair, we report the recovered period P_{rec}, asymmetric uncertainties (σ_-, σ_+), and the effective combined uncertainty $\sigma_{\rm eff} = \sqrt{(\sigma_+^2 + \sigma_-^2)/2}$.

	Band pair	$P_{\rm QhX}$ [days]	σ_- [days]	σ_+ [days]	σ_{eff} [days]	Significance
	g,r	434.67	26.29	400.93	284.6	0.92
ID = 10	*g,i*	304.17	12.95	297.40	210.4	1.00
	r,i	–	–	–	–	–
	g,r	459.48	296.60	87.18	221.4	1.00
ID = 20	*g,i*	459.48	296.60	87.18	221.4	0.98
	r,i	463.32	48.22	8.99	34.6	1.00
	g,r	296.61	4.13	18.18	13.1	0.98
ID = 25	*g,i*	296.61	4.13	18.18	13.1	1.00
	r,i	296.61	3.15	16.16	11.7	1.00

by significant statistical uncertainties, particularly at long timescales. At short scales, the SF amplitudes are low in all bands, consistent with measurement noise and weak intrinsic variability. SF increases gradually with τ up to ∼100 days, as expected for stochastic quasar variability, with systematically larger amplitudes at shorter wavelengths.

The purpose of the SF analysis is to assess whether the candidate periodicity identified in the light curves leaves a detectable imprint in the variability statistics. To guide the visual inspection, in Fig. 3, we indicate the candidate period and its harmonics (P, 2P, 3P, 4P, 5P, 6P) with vertical lines in the SF plots. The overplotted periods correspond exclusively to those derived from the SDSS light curves.

3.2.2. Color analyses

To investigate the color variability of the candidates, we searched for periodic signals in the color indices using the MBLS method. This analysis was restricted to the SDSS data, as only SDSS provides quasi-simultaneous observations (images are collected over ∼ 5 minutes, with exposure time 54 s for each band) in multiple bands suitable for constructing reliable color indices. We find that the color variability does not exhibit statistically significant periodicity, since none of the detected periods satisfy the adopted false-alarm probability threshold of 0.1%.

This result is not unexpected. Quasars exhibiting periodic or quasi-periodic variability in single-band light curves do not necessarily show coherent or strictly periodic color variations, particularly when the periodicity is transient or band-dependent (e.g. Graham et al. 2015, Charisi et al. 2018). Color changes may, instead, arise from a combination of stochastic variability, accretion-related processes, and short-lived events that affect different bands unevenly. Importantly, the absence of significant period in the color indices does not preclude phase-dependent color behavior. As illustrated in the following sections, the colors can still exhibit coherent trends when folded on the period derived from the light curves, even if they do not vary periodically as a function of time.

3.2.3. Phase-dependent color–magnitude analysis

Variability in AGN is generally stochastic and arises from accretion-related processes in a multi-temperature disk. Although AGN often show an average brighter-when-bluer behavior, such trends are typically not phase-coherent and, by themselves, do not imply periodic variability.

To test this on our candidates, we plot color–magnitude diagrams (*g-r*, *r-i*, and *g-i* versus *r*) and color code them with respect to the phase, folded on the photometric period. These diagrams are shown in Fig. 4. Within each panel, the first and last data points within a single phase cycle are connected by a dashed line, indicating the start and end of the cycle. When this separation is small, the corresponding trajectory in color–magnitude space can be interpreted as a closed loop. This interpretation is most robust for the SDSS data, owing to the observing strategy in which multi-band measurements are obtained nearly simultaneously, minimizing artificial color offsets due to time scales between bands. For this reason, the phase folding in Fig. 4 is performed using the MBLS period derived from the SDSS data alone (Block 1). If the periodic modulation is transient, this approach provides a more physically meaningful representation of the color–magnitude behavior during the interval in which the signal is most coherent.

Fig. 4 shows a clean and ordered progression with phase for most candidates (we discuss this for every source separately in Section 4). This demonstrates that the color variability is phase-locked to the same clock as the flux modulation. Such behavior disfavors purely stochastic variability and, instead, points to a single, repeatable physical mechanism. Phase-coherent color evolution of this kind is consistent with periodically driven accretion processes or geometric modulation.

3.2.4. Angle–timescale analysis of color variability

A correlated multi-band variability can be assessed using the color–variability angle as a function of timescale, as described in Sun et al. (2014). This

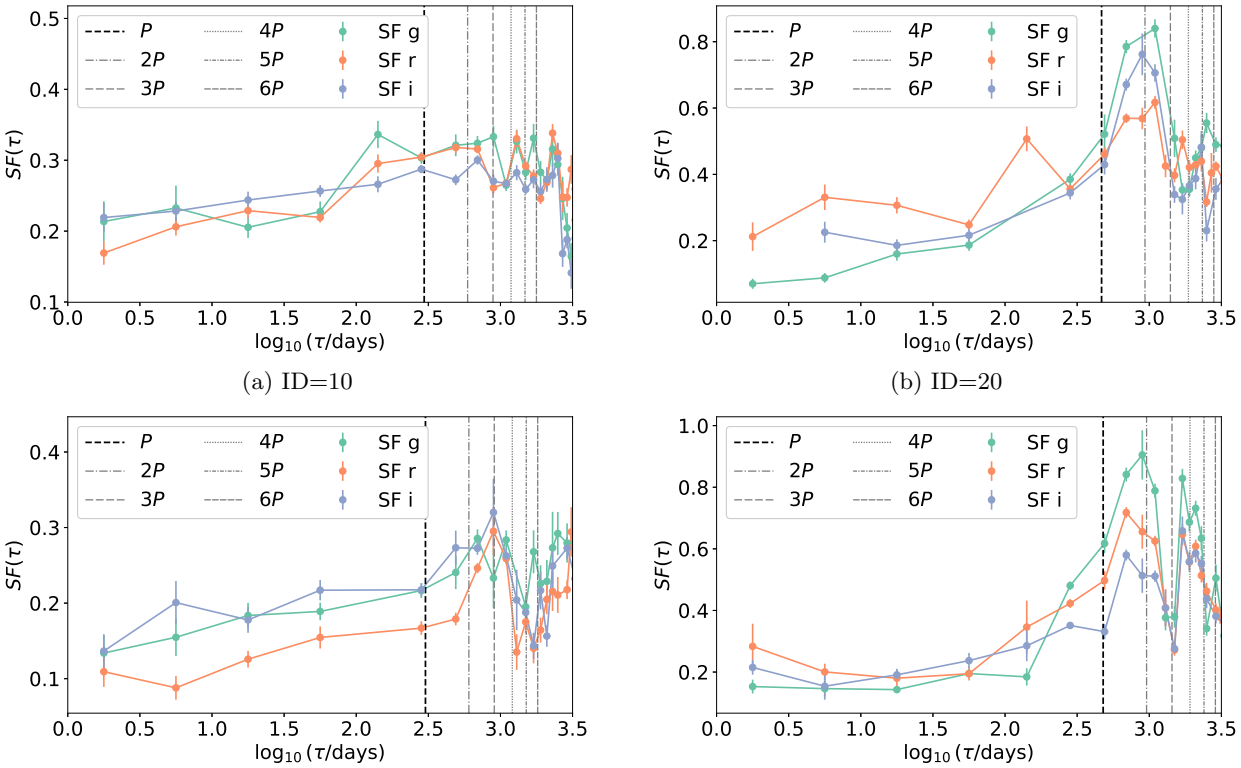

(a) ID=10 (b) ID=20

(c) ID=25 (d) ID=27

Fig. 3: SFs in the *gri* bands for the four sources analyzed in this work. Candidate period and its harmonics (P, 2P, 3P, 4P, 5P, 6P) are indicated with vertical lines (see legend). Panels (a)–(d) correspond to IDs 10, 20, 25, and 27, respectively.

statistic provides a model-independent description of the direction of variability in color–magnitude space and serves as an ensemble diagnostic of chromatic behavior.

For each source, we consider all pairs of multi-band observations separated by timescale τ and compute the color–variability angle as

$$\theta(\tau) = \arctan\left(\frac{\Delta m_r}{\Delta m_g}\right), \tag{3}$$

where Δm_g and Δm_r are the magnitude differences between two epochs in the g and r bands, respectively. The angle θ characterizes the direction of variability in color–magnitude space: $\theta = 45°$ corresponds to achromatic variability, while $\theta < 45°$ indicates bluer-when-brighter behavior. Following Sun et al. (2014), the angles are mapped onto the interval $[-45°, 135°]$.

Rather than combining all sources into an ensemble, we compute $\langle\theta(\tau)\rangle$ individually for each object, enabling us to examine how the color–variability behavior of each candidate evolves with timescale and to assess departures from the ensemble trends reported by Sun et al. (2014), particularly at long timescales. To balance time-resolution and statistical robustness across a wide range of timescales, the τ values are binned using an adaptive scheme. Logarithmic bins with width $\Delta \log \tau = 0.6$ are used at short timescales, while beyond $\tau = 200$ days, the binning transitions to linear bins of width 200 days, reducing the density of bins at long timescales. Only bins containing at least five valid pairs are retained. For each bin, the mean angle $\langle\theta(\tau)\rangle$ and its uncertainty are computed from the distribution of individual angle measurements. Timescales are restricted to $\tau \geq 1$ day and to a maximum of 80% of the total temporal baseline of each source. Vertical reference lines are overplotted at the photometric period P and at selected harmonics, including integer multiples from $2P$ up to $8P$, to facilitate comparison between characteristic color-variability timescales and the candidate periodic modulation. Uncertainties on $\langle\theta(\tau)\rangle$ are estimated conservatively as the standard error of the mean within each timescale bin.

Sun et al. (2014) demonstrated that, when considering large ensembles of quasars, color variability exhibits a clear timescale dependence: variability is strongly chromatic at short timescales and becomes progressively more achromatic toward longer timescales. In particular, for time lags $\tau \gtrsim 100$ days, the mean color–variability angle approaches $\theta \approx 45°$, consistent with nearly achromatic variability. Although their analysis was based on ensemble statistics, we here adopt the same formalism to exam-

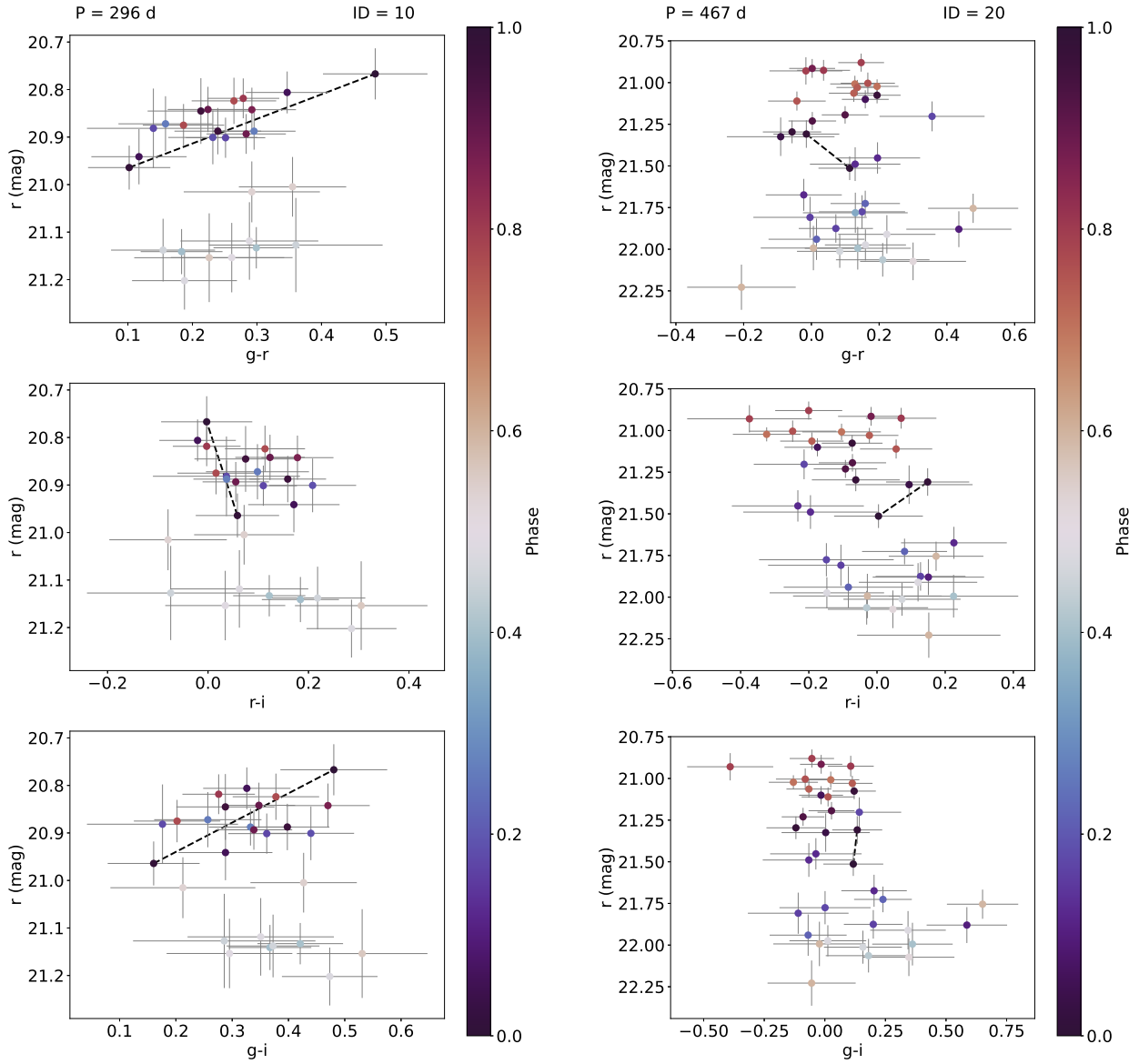

Fig. 4: Color–magnitude diagrams for each source. The color bar presents the phase obtained using MBLS periods derived from the SDSS dataset. The dashed line connects the first and last phases of each cycle.

ine whether a similar behavior is present in individual sources and, specifically, whether the candidate periodic signals identified in the light curves manifest distinct color–variability signatures when viewed through this framework (Sun et al. 2014). We discuss the obtained results for every source separately in Section 4.

4. DISCUSSION

Tables 2 and 4 summarize the periods derived using the MBLS and QhX methods. Below, we discuss each candidate individually.

4.1. Object ID = 10

The quasar with ID = 10 has a substantially larger number of observations from PS1, DES, and ZTF compared to the other sources in the sample, owing to its being the brightest object considered in this work. Nevertheless, despite its relative brightness, the source remains intrinsically faint, and its light curves (Fig. 1a) are characterized by large scatter and a low variability amplitude.

Periods derived from the full light curves are consistent across the different methods applied. However, when the data are subdivided into temporal blocks (Block 1, 2, and 3; see Table 2), the resulting MBLS periods ($P_{\rm MBLS}$) differ markedly. In particu-

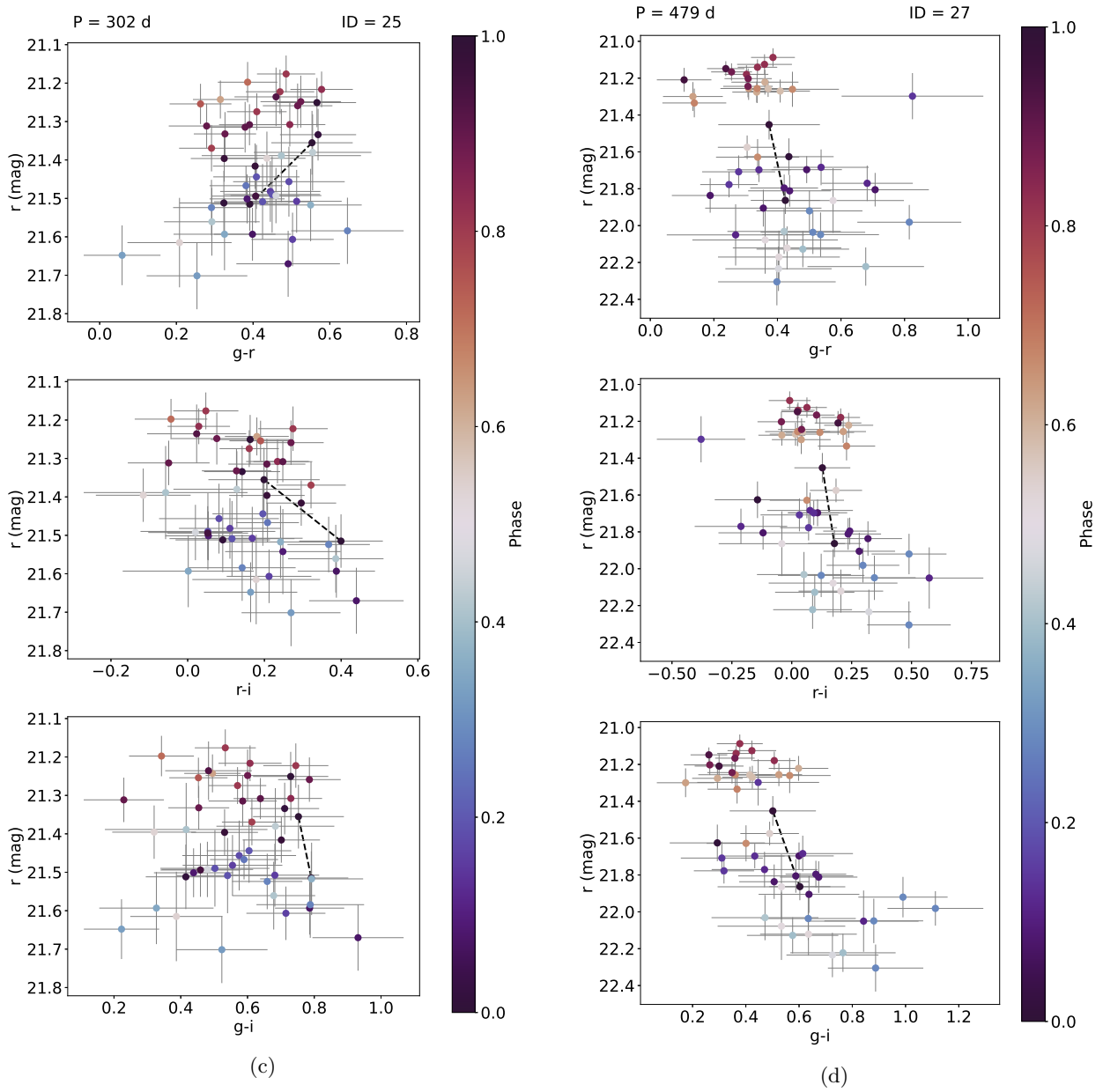

Fig. 4: Continued.

lar, the period detected in the SDSS-only data (Block 1) is flagged as lying close to a prominent peak in the window function and must therefore be interpreted with caution. The period obtained from ZTF alone (Block 3) is not considered reliable owing to the limited number of data points and its failure to satisfy the false-alarm probability criterion. Similarly, the apparent periodicity detected in Block 2 is also found to coincide with a window-function peak and does not meet the significance threshold.

Taken together, these results suggest that the detected periodic signal is not persistent over the full temporal baseline but may instead be temporally localized, potentially associated with the epoch covered by the SDSS observations. Interestingly, the period derived from the full light curves is formally significant, does not coincide with prominent seasonal aliases, and differs from the SDSS-only period, indicating that the combined data favor a distinct, longer-timescale modulation.

Further insight is provided by the phase-coded color–magnitude diagrams constructed using only the SDSS data and its corresponding period (Fig. 4a). These diagrams reveal a clear phase-dependent structure across all color combinations, arguing against a purely stochastic origin of the variability. In particular, the r–i versus r diagram exhibits a tentative closed loop, suggesting that during the SDSS observing epoch, the source may undergone a transient, quasi-periodic variability phase.

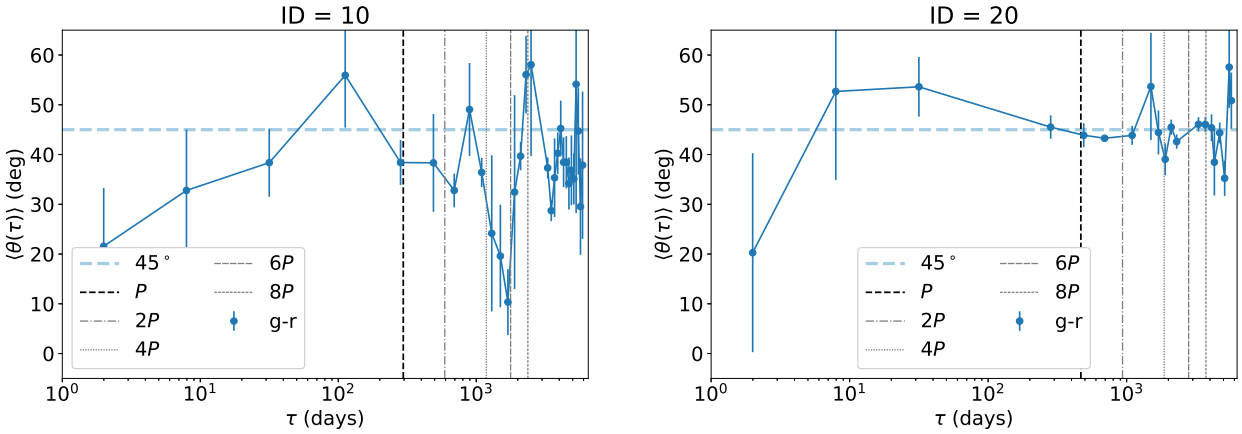

(a) ID=10

(b) ID=20

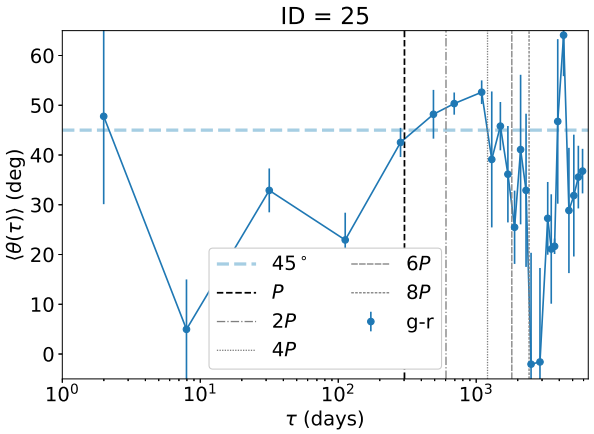

(c) ID=25

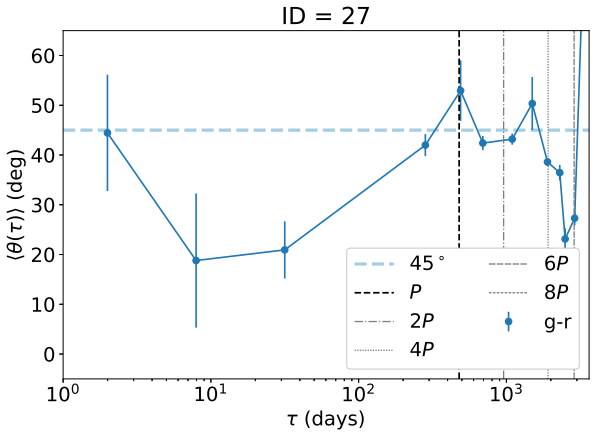

(d) ID=27

Fig. 5: Timescale dependence of the color–variability angle. The mean color–variability angle $\langle\theta(\tau)\rangle$ is computed from the SDSS epoch pairs and binned logarithmically in τ. The dashed horizontal line marks the achromatic expectation at $\theta = 45°$. Vertical lines represent the photometric period P and at selected harmonics, including integer multiples from $2P$ up to $8P$.

The absence of statistically significant minima in the SF (see Fig. 3a) indicates that strictly phase-coherent periodic variability is not present in the color light curves. However, the pronounced long-timescale structure observed in the $\theta(\tau)$ diagnostic (see Fig. 5a) reveals coherent chromatic variability patterns, likely associated with slowly evolving accretion disk processes rather than a stable periodic driver. This behavior motivates continued monitoring to assess long-term coherence and physical origin.

4.2. Object ID = 20

The source with ID = 20 (see Table 2) exhibits large-amplitude variability exceeding 1 magnitude in all bands. This amplitude is consistently recovered in the analysis of the full light curve and in Block 1, and is broadly consistent with Block 3, although the latter suffers from a small number of data points, particularly in the *gi* bands. In contrast, Block 2 shows a somewhat reduced variability amplitude. Such amplitude differences may reflect changes in the dominant variability mechanism over time or may be influenced by survey-specific cadence and photometric uncertainties.

The periodicity analysis reveals broadly good agreement between the period derived from the full light curves and that obtained using the SDSS data alone. In contrast, Block 2 yields a statistically insignificant period, with its periodogram peak lying close to a prominent feature in the window function, rendering this detection unreliable. The ZTF-only analysis (Block 3) recovers a period that differs from the SDSS and full-light-curve values, yet remains statistically significant. The main caveat is that the corresponding periodogram peak is again located near a window-function peak, suggesting possible sensitivity to cadence-related aliases.

Visual inspection of Fig. 1b shows that the PS1 data broadly follow the sinusoidal model, while the DES and ZTF data display an apparent phase offset

relative to the same model. Notably, the period derived from ZTF alone differs from that inferred from SDSS and the full light curve analysis. Nevertheless, the ZTF data reveal a clear, recurrent modulation with comparable amplitude over multiple cycles, particularly in the r band, indicating that the periodic behavior re-emerges at later epochs rather than being confined to a single observing window. This recurrence argues against a purely stochastic origin and suggests an underlying physical process capable of producing quasi-periodic variability over extended timescales.

Additional support for robustness of this periodic interpretation comes from the color–magnitude analysis. The phase-coded color–magnitude diagrams (see Fig. 4b) show a well-organized phase distribution, and this source is the only candidate in the sample to exhibit a particularly clear loop-like structure. Such loop behavior is indicative of coherent, phase-dependent spectral changes and strongly suggests that the SDSS-detected periodicity is intrinsic to the source. However, due to the limited number of ZTF observations in the gi bands, it is not yet possible to confirm whether the later-time periodic modulation is accompanied by similarly coherent color evolution.

Although the θ–timescale analysis does not reveal a deviation from the expected achromatic behavior (see Fig. 5b), the SF analysis exhibits pronounced features at longer timescales, with a minimum coinciding with an integer multiple of the period, specifically at $4P$ (see Fig. 3b).

4.3. Object ID = 25

The source with ID = 25 exhibits the smallest variability amplitude in the sample (Table 2). The periods derived from the SDSS data and from the full light-curve analysis are mutually consistent, whereas no statistically significant periodic signal is recovered in Blocks 2 and 3. This result should be interpreted with caution, as both blocks—particularly Block 3—contain very few data points. Even when the PS1, DES, and ZTF observations are combined, the total number of measurements remains roughly 50% lower than for SDSS alone, substantially limiting the reliability of any period determination outside the SDSS epoch.

In the ZTF g band, the source displays an apparent variation of up to ∼0.8 mag; however, the characteristic timescale of this variability is visibly much longer than the periods inferred from the SDSS data. Given that the source is intrinsically faint and close to the ZTF sensitivity limit, the sparse sampling and large photometric uncertainties preclude a reliable period measurement, and the variability can only be assessed qualitatively. In the i band, the PS1 data show a significant variability amplitude that is broadly consistent with a sinusoidal trend, but here again, the limited number of observations prevents an independent and robust period estimate.

Taken together, these findings suggest that the periodic signal detected in the SDSS data is either transient and confined to that observing epoch or represents a false positive arising from stochastic variability. Visual inspection of the light curves (Fig. 1c) favors the latter interpretation, as no clear or repeatable modulation is evident across the full temporal baseline.

The color–magnitude analysis (Fig. 4c) further supports a cautious interpretation. Compared to the other sources in the sample, the phase separation in the color–magnitude diagrams is weak. Although a mild trend is present, with bluer colors preferentially associated with brighter magnitudes, the effect is small compared to the overall scatter. A tentative indication of loop-like behavior appears in the r–i versus r diagram, but the large scatter dominates the distribution. Overall, the combination of low variability amplitude, sparse multi-band coverage, and weak chromatic coherence suggests that this source is unlikely to be a strong candidate for transient periodic behavior.

However, this conclusion is partially challenged by the results of the SF and color–variability angle analyses. The SF exhibits pronounced minima at time lags corresponding to 4P or 5P (depending on the band), a feature that is difficult to reproduce with purely stochastic variability. Consistently, the $\theta(\tau)$ analysis reveals systematic deviations from the behavior expected for typical quasars: rather than converging toward achromatic variability at long timescales, as found in ensemble studies by Sun et al. (2014), the color–variability angle remains significantly offset from $\theta \approx 45°$ at time lags comparable to 8P. This behavior suggests that, despite the weak and noisy color–magnitude loops, the variability in this source is organized in a manner that departs from the canonical quasar trend and may be linked to the same mechanism producing the periodic modulation.

4.4. Object ID = 27

The quasar with ID = 27 is the faintest source in the sample, with median g, r, and i magnitudes of approximately 22.0, 21.7, and 21.5 mag, respectively (Table 2). Despite its faintness, the source exhibits a variability amplitude of about 1 mag.

The periods derived from the full light-curve analysis and from the SDSS data (Block 1) are mutually consistent. In contrast, no statistically significant periodic signal is recovered in Blocks 2 and 3. It is worth noting, however, that the period inferred from the SDSS data lies close to a prominent peak in the window function and, therefore, requires careful interpretation.

Visual inspection of the light curves (Fig. 1d) reveals that in the i band, the PS1 and DES data – PS1 particularly – exhibit large-amplitude variability that is well described by the sinusoidal model. In the g and r bands, the number of available data points

is too small to draw meaningful conclusions. The ZTF data also show large-amplitude variations that broadly align with the sinusoidal model, suggesting that the observed periodicity may be intrinsic to the source. However, due to the faintness of the quasar and the resulting photometric uncertainties, the ZTF data alone do not allow for a robust, independent confirmation of the period. Nevertheless, the persistence of a large variability amplitude across the full temporal baseline supports the interpretation of an underlying, coherent modulation.

The color–magnitude diagrams shown in Fig. 4d provide additional support for this interpretation. A strong phase-dependent structure is evident, particularly for this source, which also exhibits the largest modulation amplitude. In the g-i versus r panel, there is a clear indication of loop-like behavior, consistent with coherent, phase-dependent spectral changes. A pronounced BWB trend, typical of quasar variability, is also present.

Taken together, these results suggest that ID = 27 may host a periodic or quasi-periodic signal that persists over much of the observed timespan. However, due to the extreme faintness of the source and the limited multi-band coverage—especially in the gr bands outside SDSS—the periodicity cannot yet be tightly constrained. At minimum, the source appears to exhibit transiently periodic behavior during the SDSS epoch. Extending the color–magnitude analysis to the PS1 data would be highly valuable, but the current lack of sufficiently dense gr-band observations prevents such an investigation at present.

Similarly to the candidate with ID = 20, this source shows consistent support from the auxiliary variability diagnostics. The SF exhibits well-defined minima at timescales corresponding to $\sim 3P$ and, at longer timescales, near $\sim 5P$–$6P$ (see Fig. 3d), with the exact location depending on the photometric band. The $\theta(\tau)$ analysis reveals a compatible pattern, with systematic features emerging at comparable multiples of the candidate period, particularly around $\sim 6P$ (see Fig. 5d). At the same time, the overall variation in the color–variability angle is more modest than in the other two sources with similarly robust periodic signatures, indicating a weaker but still coherent chromatic response.

5. SUMMARY AND CONCLUSIONS

In this work, we investigated four faint (∼21–22 mag) quasar candidates for periodic or quasi-periodic variability originally identified by F23, using updated multi-survey light curves combining the SDSS, PS1, DES, and ZTF data. Beyond standard period searches, we applied a set of complementary, physically motivated diagnostics—including phase-resolved color–magnitude diagrams, the SF analysis, and the color–variability angle $\theta(\tau)$—to estimate the robustness and nature of the candidate periodic signals.

Our analysis shows that reliance on light-curve periodicity alone provides an incomplete and potentially misleading picture, particularly in the regime of faint quasars where sparse sampling, heterogeneous cadences, and red-noise–dominated variability are prevalent. While all four sources show limitations when examined using individual diagnostics, all of them exhibit potentially coherent, non-stochastic behavior when multiple lines of evidence are considered together.

The candidates with IDs 20 and 27 emerge as the strongest cases in the sample for at least transient periodic behavior. For both sources, variability patterns detected in the SDSS data reappear at later epochs, and their color–magnitude diagrams display clear, phase-dependent loop-like structures indicative of coherent spectral evolution. These findings are further supported by the SF analysis, which reveal systematic features at integer multiples of the candidate periods. Such behavior is difficult to reconcile with purely stochastic variability and instead points to an possible intrinsic, organized modulation, making these two quasars compelling targets for future spectroscopic monitoring.

The remaining two candidates (IDs 10 and 25) exhibit lower variability amplitudes and weaker consistency between different temporal blocks, and would likely be classified as ambiguous or weak based on period searches alone. Nevertheless, both sources show notable departures from the canonical quasar behavior when examined with supporting diagnostics. In particular, ID = 10 displays coherent phase-dependent color structure and a pronounced feature in the $\theta(\tau)$ analysis at long timescales, while ID = 25 exhibits SF minima and color–variability angles that deviate from the achromatic trend expected at large timescales. Although these signatures do not constitute definitive evidence for periodicity, they indicate organized variability that cautions against dismissing such sources as false positives on the basis of a single test.

Taken together, our results demonstrate that periodic or quasi-periodic behavior in quasars—especially when transient—may manifest differently across diagnostics and timescales. The combined use of light-curve periodicity, color–magnitude evolution, SFs, and color–variability angles provides a more robust framework for evaluating candidate periodic AGN. This multi-diagnostic approach is particularly valuable given that evaluations based mainly on photometric diagnostics alone may overlook astrophysically informative behavior that becomes apparent only through spectroscopic follow-up (e.g. Fatović et al. 2025). As large time-domain surveys continue to expand the sample of faint, variably sampled quasars, such an integrated methodology will be essential for prioritizing the most promising systems and for avoiding the premature rejection of genuinely interesting sources.

Looking ahead, upcoming surveys such as LSST will provide unprecedented depth and cadence for studies of faint AGN. Although strictly simultaneous multi-band observations remain limited, the typical inter-band separations of 1–3 days will still permit measurements obtained within short time windows (e.g., $\lesssim$1 day) to be combined into reliable color indices. Together with LSST's high cadence, this observing strategy will enable robust phase-resolved color analyses similar to those employed in this work. Our results highlight the diagnostic power of coherent, phase-dependent color behavior—particularly loop-like structures and long-timescale departures from achromatic variability—as an important complement to traditional light-curve–based searches for periodicity in quasars.

Acknowledgements – M.F. and D.D. acknowledge the financial support by Italian Ministry for Education University and Research (MIUR) grant PRIN 2022 2022383WFT "SUNRISE" and from the Timedomes grant within the "INAF 2023 Finanziamento della Ricerca Fondamentale". D.D. acknowledges PON R&I 2021, CUP E65F21002880003, and Fondi di Ricerca di Ateneo (FRA), linea C, progetto TORNADO.

A.B.K. and D.I. acknowledge funding provided by the University of Belgrade - Faculty of Mathematics (the contract 451-03-33/2026-03/200104) through the grants by the Ministry of Science, Technological Development and Innovation of the Republic of Serbia, and the support of the HPC AI Platform of Office for Information Technologies and e-Government of Republic Serbia.

Based on observations obtained with the Samuel Oschin Telescope 48-inch and the 60-inch Telescope at the Palomar Observatory as part of the Zwicky Transient Facility project. ZTF is supported by the National Science Foundation under Grants No. AST-1440341 and AST-2034437 and a collaboration including current partners Caltech, IPAC, the Oskar Klein Center at Stockholm University, the University of Maryland, University of California, Berkeley, the University of Wisconsin at Milwaukee, University of Warwick, Ruhr University, Cornell University, Northwestern University and Drexel University. Operations are conducted by COO, IPAC, and UW.

REFERENCES

Abbott, T. M. C., Adamów, M., Aguena, M., et al. 2021, ApJS, 255, 20

Begelman, M. C., Blandford, R. D. and Rees, M. J. 1980, Natur, 287, 307

Boroson, T. A. and Lauer, T. R. 2009, Natur, 458, 53

Britzen, S., Zajaček, M., Gopal-Krishna, et al. 2023, ApJ, 951, 106

Caplar, N., Lilly, S. J. and Trakhtenbrot, B. 2017, ApJ, 834, 111

Chambers, K. C., Magnier, E. A., Metcalfe, N., et al. 2016, arXiv:1612.05560

Charisi, M., Bartos, I., Haiman, Z., et al. 2016, MNRAS, 463, 2145

Charisi, M., Haiman, Z., Schiminovich, D. and D'Orazio, D. J. 2018, MNRAS, 476, 4617

Chen, Y.-J., Zhai, S., Liu, J.-R., et al. 2024, MNRAS, 527, 12154

Dark Energy Survey Collaboration, Abbott, T., Abdalla, F. B., et al. 2016, MNRAS, 460, 1270

De Cicco, D., Paolillo, M., Falocco, S., et al. 2019, A&A, 627, A33

De Cicco, D., Bauer, F. E., Paolillo, M., et al. 2022, A&A, 664, A117

De Rosa, A., Vignali, C., Bogdanović, T., et al. 2019, NewAR, 86, 101525

de Vries, W. H., Becker, R. H., White, R. L. and Loomis, C. 2005, AJ, 129, 615

Deng, H. 2026, PhRvD, 113, 083021

D'Orazio, D. J., Haiman, Z. and MacFadyen, A. 2013, MNRAS, 436, 2997

D'Orazio, D. J., Haiman, Z. and Schiminovich, D. 2015, Natur, 525, 351

El-Badry, K., Hogg, D. W. and Rix, H.-W. 2026, PASP, 138, 024102

Emmanoulopoulos, D., McHardy, I. M. and Uttley, P. 2010, MNRAS, 404, 931

Eracleous, M. and Halpern, J. P. 1994, ApJS, 90, 1

Falocco, S., Paolillo, M., Covone, G., et al. 2015, A&A, 579, A115

Farris, B. D., Duffell, P., MacFadyen, A. I. and Haiman, Z. 2014, ApJ, 783, 134

Fatović, M., Palaversa, L., Tisanić, K., et al. 2023, AJ, 165, 138

Fatović, M., Ilić, D., Kovačević, A. B., et al. 2025, A&A, 695, A208

Flewelling, H. A., Magnier, E. A., Chambers, K. C., et al. 2020, ApJS, 251, 7

Graham, M. J., Djorgovski, S. G., Stern, D., et al. 2015, Natur, 518, 74

Graham, M. J., Djorgovski, S. G., Drake, A. J., et al. 2017, MNRAS, 470, 4112

Guo, H., Liu, X., Shen, Y., et al. 2019a, MNRAS, 482, 3288

Guo, H., Sun, M., Liu, X., et al. 2019b, ApJL, 883, L44

Ivezić, Ž. and MacLeod, C. 2014, in IAU Symposium, Vol. 304, Multiwavelength AGN Surveys and Studies, ed. A. M. Mickaelian and D. B. Sanders, 395

Ivezic, Ž., Lupton, R. H., Juric, M., et al. 2004, in IAU Symposium, Vol. 222, The Interplay Among Black Holes, Stars and ISM in Galactic Nuclei, ed. T. Storchi-Bergmann, L. C. Ho and H. R. Schmitt, 525

Ivezić, Ž., Smith, J. A., Miknaitis, G., et al. 2007, AJ, 134, 973

Ivezić, Ž., Kahn, S. M., Tyson, J. A., et al. 2019, ApJ, 873, 111

Janiuk, A. and Czerny, B. 2011, MNRAS, 414, 2186

Kasliwal, V. P., Vogeley, M. S., Richards, G. T., Williams, J. and Carini, M. T. 2015, MNRAS, 453, 2075

Kelly, B. C., Bechtold, J. and Siemiginowska, A. 2009, ApJ, 698, 895
Kovačević, A. B., Pérez-Hernández, E., Popović, L. Č., et al. 2018, MNRAS, 475, 2051
Kovačević, A. B., Popović, L. Č., Simić, S. and Ilić, D. 2019, ApJ, 871, 32
Kovačević, A. B., Popović, L. Č. and Ilić, D. 2020, OAst, 29, 51
Kovačević, A. B., Ilić, D., Popović, L. Č., et al. 2021, MNRAS, 505, 5012
Kovačević, A. B., Nina, A., Popović, L. Č. and Radovanović, M. 2022, Mathematics, 10
Kozłowski, S. 2016, ApJ, 826, 118
Kozłowski, S., Kochanek, C. S., Udalski, A., et al. 2010, ApJ, 708, 927
Krishnan, S., Markowitz, A. G., Schwarzenberg-Czerny, A. and Middleton, M. J. 2021, MNRAS, 508, 3975
Lewis, K. T., Eracleous, M. and Storchi-Bergmann, T. 2010, ApJS, 187, 416
Liao, W.-T., Chen, Y.-C., Liu, X., et al. 2021, MNRAS, 500, 4025
Liska, M., Hesp, C., Tchekhovskoy, A., et al. 2018, MNRAS, 474, L81
LSST Science Collaboration, Abell, P. A., Allison, J., et al. 2009, arXiv:0912.0201
MacLeod, C. L., Ivezić, Ž., Kochanek, C. S., et al. 2010, ApJ, 721, 1014
Madore, B. F. 1985, ApJ, 298, 340
Masci, F. J., Laher, R. R., Rusholme, B., et al. 2019, PASP, 131, 018003
Paolillo, M. and Papadakis, I. 2025, Nuovo Cimento Rivista Serie, 48, 537
Popović, L. Č., Shapovalova, A. I., Ilić, D., et al. 2014, A&A, 572, A66
Qian, S. J., Britzen, S., Witzel, A., Krichbaum, T. P. and Kun, E. 2018, A&A, 615, A123
Rigamonti, F., Bertassi, L., Buscicchio, R., et al. 2025, A&A, 702, A242
Runnoe, J. C., Cales, S., Ruan, J. J., et al. 2016, MNRAS, 455, 1691
Sánchez-Sáez, P., Lira, P., Mejía-Restrepo, J., et al. 2018, ApJ, 864, 87
Schmidt, K. B., Rix, H.-W., Shields, J. C., et al. 2012, ApJ, 744, 147
Sesar, B., Ivezić, Ž., Grammer, S. H., et al. 2010, ApJ, 708, 717
Shen, Y. and Loeb, A. 2010, ApJ, 725, 249
Simm, T., Salvato, M., Saglia, R., et al. 2016, A&A, 585, A129
Śniegowska, M., Trakhtenbrot, B., Makrygianni, L., et al. 2025, ApJ, 989, 173
Stone, Z., Shen, Y., Burke, C. J., et al. 2022, MNRAS, 514, 164
Sudan, M., Chand, H., Wiita, P. J. and Kumar, R. 2025, MNRAS, 543, 121
Sun, Y.-H., Wang, J.-X., Chen, X.-Y. and Zheng, Z.-Y. 2014, ApJ, 792, 54
Szabó, R., Ivezić, Ž., Kiss, L. L., et al. 2014, ApJ, 780, 92
Thanjavur, K., Ivezić, Ž., Allam, S. S., et al. 2021, MNRAS, 505, 5941
Ulrich, M.-H., Maraschi, L. and Urry, C. M. 1997, ARA&A, 35, 445
Vanden Berk, D. E., Wilhite, B. C., Kron, R. G., et al. 2004, ApJ, 601, 692
VanderPlas, J. T. and Ivezić, Ž. 2015, ApJ, 812, 18
Vaughan, S., Uttley, P., Markowitz, A. G., et al. 2016, MNRAS, 461, 3145
Witt, C. A., Charisi, M., Taylor, S. R. and Burke-Spolaor, S. 2022, ApJ, 936, 89
York, D. G., Adelman, J., Anderson, Jr., J. E., et al. 2000, AJ, 120, 1579
Yu, W., Richards, G. T., Ruan, J. J., et al. 2025, ApJ, 992, 130
Zu, Y., Kochanek, C. S., Kozłowski, S. and Udalski, A. 2013, ApJ, 765, 106

ТЕСТИРАЊЕ НОВИХ МЕТОДА ЗА ДИЈАГНОСТИКУ ПЕРИОДИЧНОСТИ КВАЗАРА У ЕРИ ВЕЛИКИХ ПРЕГЛЕДА НЕБА

Marta Fatović[1,2,3], **Анђелка Б. Ковачевић**[4], **Драгана Илић**[4,5] **and Demetra De Cicco**[1]

[1] *Dipartimento di Fisica "Ettore Pancini", Università di Napoli Federico II, Via Cintia 80126, Naples, Italy*
E–mail: *marta.fatovic@unina.it*

[2] *Ruđer Bošković Institute, Bijenička cesta 54, 10000 Zagreb, Croatia*

[3] *INAF – Osservatorio Astronomico di Capodimonte, Via Moiariello 16, 80131 Naples, Italy*

[4] *Катедра за астрономију, Математички факултет, Универзитет у Београду, Студентски трг 16, 11000 Београд, Србија*

[5] *Hamburger Sternwarte, Universität Hamburg, Gojenbergsweg 112, D-21029 Hamburg, Germany*

УДК 524.7–337 + 524.6–76
Оригинални научни рад

У овом раду анализирамо променљивост четири квазара који су раније издвојени као кандидати за периодичну променљивост. Криве сјаја допунили смо новим подацима из прегледа неба Pan-STARRS1 (PS1), додатним посматрањима из каталога *Zwicky Transient Facility* (ZTF), као и архивским подацима из *Dark Energy Survey* (DES), који нису били укључени у претходну анализу. Тиме су значајно унапређени временско покривање подацима и каденца узорковања кривих сјаја. Периодичност поново процењујемо применом две независне методе за претрагу периода, што омогућава непосредно поређење добијених периода на различитим скуповима података и временским интервалима, као и испитивање њихове осетљивости на ефекте узорковања и стохастичку променљивост. Поред тога, анализирамо структурну функцију, фазно понашање на дијаграмима боја–магнитуда и временску еволуцију боја како бисмо испитали да ли су уочени периодични сигнали праћени другим кохерентним (хроматским) облицима променљивости. Ова обједињена анализа представља методолошки оквир за анализу података будућих великих временских прегледа неба у временском домену, са циљем испитивања робусности, постојаности и физичке природе могуће периодичности код квазара слабог сјаја.